

Dynamically tunable terahertz passband filter based on metamaterials integrated with a graphene middle layer

MaoSheng Yang(杨茂生), LanJu Liang(梁兰菊), DeQuan Wei(韦德泉), Zhang Zhang(张璋), Xin Yan(闫昕), Meng Wang(王猛), JianQuan Yao(姚建铨)

Citation: Chin. Phys. B . 2018, 27(9): 098101. **doi:** 10.1088/1674-1056/27/9/098101

Journal homepage: http://cpb.iphy.ac.cn; http://iopscience.iop.org/cpb

What follows is a list of articles you may be interested in

Robust stability characterizations of active metamaterials with non-Foster loads

Yi-Feng Fan(范逸风), Yong-Zhi Sun(孙永志)

Chin. Phys. B . 2018, 27(2): 028102. **doi:** 10.1088/1674-1056/27/2/028102

Polarization-insensitive unidirectional spoof surface plasmon polaritons coupling by gradient metasurface

Hong-yu Shi(施宏宇), An-xue Zhang(张安学), Jian-zhong Chen(陈建忠), Jia-fu Wang(王甲富), Song Xia(夏颂), Zhuo Xu(徐卓)

Chin. Phys. B . 2016, 25(7): 078105. **doi:** 10.1088/1674-1056/25/7/078105

Enhanced circular dichroism based on the dual-chiral metamaterial in terahertz regime

Jian Shao(邵健), Jie Li(李杰), Ying-Hua Wang(王英华), Jia-Qi Li(李家奇), Zheng-Gao Dong(董正高), Lin Zhou(周林)

Chin. Phys. B . 2016, 25(5): 058103. **doi:** 10.1088/1674-1056/25/5/058103

Tunable electromagnetically induced transparency at terahertz frequencies in coupled graphene metamaterial

Ding Guo-Wen, Liu Shao-Bin, Zhang Hai-Feng, Kong Xiang-Kun, Li Hai-Ming, Li Bing-Xiang, Liu Si-Yuan, Li Hai

Chin. Phys. B . 2015, 24(11): 118103. **doi:** 10.1088/1674-1056/24/11/118103

Tri-band transparent cross-polarization converters using a chiral metasurface

Shi Hong-Yu, Li Jian-Xing, Zhang An-Xue, Wang Jia-Fu, Xu Zhuo

Chin. Phys. B . 2014, 23(11): 118101. **doi:** 10.1088/1674-1056/23/11/118101

Dynamically tunable terahertz passband filter based on metamaterials integrated with a graphene middle layer*

MaoSheng Yang(杨茂生)[1,2,4], LanJu Liang(梁兰菊)[1,2,3,4,†], DeQuan Wei(韦德泉)[1,4,‡], Zhang Zhang(张璋)[1,2,3,4], Xin Yan(闫昕)[1,2,3,4], Meng Wang(王猛)[1,4], and JianQuan Yao(姚建铨)[1,3,4]

[1] *School of Opto-electronics Engineering, Zaozhuang University, Zaozhuang* 277160, *China*

[2] *College of Precision Instrument and Opto-electronics Engineering, Tianjin University, Tianjin* 300072, *China*

[3] *Key Laboratory of Optoelectronic Information Science and Technology (Ministry of Education), Tianjin University, Tianjin* 300072 ,*China*

[4] *Key Laboratory of Optoelectronic Information Processing and Display in Universities of Shandong, Zaozhuang University, Zaozhuang* 277160, *China*

(Received 2 February 2018; revised manuscript received 24 June 2018; published online 28 August 2018)

The dynamic tunability of a terahertz (THz) passband filter was realized by changing the Fermi energy (E_F) of graphene based on the sandwiched structure of metal–graphene–metal metamaterials (MGMs). By using plane wave simulation, we demonstrated that the central frequency (f_0) of the proposed filter can shift from 5.04 THz to 5.71 THz; this shift is accompanied by a 3 dB bandwidth (Δf) decrease from 1.82 THz to 0.01 THz as the E_F increases from 0 to 0.75 eV. Additionally, in order to select a suitable control equation for the proposed filter, the curves of Δf and f_0 under different graphene E_F were fitted using five different mathematical models. The fitting results demonstrate that the DoseResp model offers accurate predictions of the change in the 3 dB bandwidth, and the Quartic model can successfully describe the variation in the center frequency of the proposed filter. Moreover, the electric field and current density analyses show that the dynamic tuning property of the proposed filter is mainly caused by the competition of two coupling effects at different graphene E_F, i.e., graphene–polyimide coupling and graphene–metal coupling. This study shows that the proposed structures are promising for realizing dynamically tunable filters in innovative THz communication systems.

Keywords: metamaterial, terahertz, filter, mathematical model, tunability, graphene

PACS: 81.05.xj, 42.25.Fx, 84.30.Vn, 43.58.Kr **DOI:** 10.1088/1674-1056/27/9/098101

1. Introduction

Terahertz (THz) waves have shown promising technological potential for use in many applications, such as medical imaging, biomolecular sensing, fingerprint detection, and identification.[1–7] However, using THz devices to effectively manipulate THz waves for increasing their suitability to more applications is a challenge. The control of THz radiation by natural materials is very inefficient owing to the weak electromagnetic responses of these materials.[8,9] Recently, metamaterials, which are composed of artificial sub-wavelength structures, were proposed; the effective permittivity and/or permeability of these materials can be altered in large degrees of freedom owing to their extraordinary electromagnetic properties, such as a negative refractive index, which do not exist in natural materials.[2,10–16] Such properties of metamaterials allow for the development of an efficient method for realizing potentially functional components for THz technology. THz metamaterial-based filters have been reported in other research works owing to their superior properties.[17,18] However, the narrow operational bandwidth and signal distortion of these filters significantly limit the development of functional communication devices and limit their applications in many practical fields.[19] Furthermore, the traditional metamaterial-based filters cannot tune the electromagnetic properties of THz waves dynamically in actual cases. Although the coplanar hybridization of graphene with metamaterials has been reported because of the tunable Fermi level of graphene, E_F, the transmission efficiency of filters using such materials is greatly reduced owing to the large loss in THz frequency. This makes it difficult to apply THz filters in THz communication systems.[20–22]

In this study, we demonstrate a unique platform for dynamically tunable THz filters based on metal–graphene–metal metamaterials (MGMs), in which the passband frequency regions are tuned over a wide range. To examine the corresponding transmission spectra of the proposed filters, a THz frequency domain calculation was carried out. The results indicated that MGMs can dynamically tune THz transmission spectra with only a slight reduction in efficiency. The trans-

*Project supported by the National Natural Science Foundation of China (Grant Nos. 61701434, 61735010, and 61675147), the Open Fund of the Key Laboratory of Optoelectronic Information Technology, Ministry of Education (Tianjin University), China, the Key Laboratory of Optoelectronic Information Functional Materials and Micro-Nano devices in Zaozhuang, China, the China Postdoctoral Science Foundation (Grant No. 2015M571263), the Natural Science Foundation of Shandong Province, China (Grant Nos. ZR2017MF005 and ZR2018LF001), Project of Shandong Province Higher Education Science and Technology Program, China (Grant No. J17KA087), the Program of Independent and Achievement Transformation Plan for Zaozhuang, China (Grant Nos. 2016GH19 and 2016GH31), and Zaozhuang Engineering Research Center of Terahertz, China.

†Corresponding author. E-mail: lianglanju123@163.com

‡Corresponding author. E-mail: 13561121758@163.com

© 2018 Chinese Physical Society and IOP Publishing Ltd

mission spectra of MGMs largely shift from 2 THz to 4 THz as a result of tuning the E_F of graphene. Instead, few changes in the range 4–8 THz were observed. In addition, to select a suitable control equation for the proposed filter, the curves of the 3 dB bandwidth (Δf) and the center frequency (f_0) of the graphene E_F were fitted using five different mathematical models. The DoseResp model offers accurate predictions for control of the 3 dB bandwidth, and the Quartic model can successfully describe the variation in the center frequency of THz passband filters. Finally, the results indicated that the proposed structure exhibited satisfactory performance in the THz region, particularly in terms of tunability.

2. Structural design and simulations

The periodic structures of the metamaterial are schematically shown in Fig. 1(a); the bottom structure and design of an individual unit cell of the metamaterial are shown in Figs. 1(b) and 1(c), respectively. The unit cell contained a monolayer graphene sheet sandwiched by a polyimide (PI) layer of 10 μm. The material of the top layer was the same as that of the bottom layer, which was composed of a 200-nm-thick metal film with an electrical conductivity of 4.09×10^7 S/cm; the monolayer graphene sheet was treated as a zero-thickness conductive medium.[23]

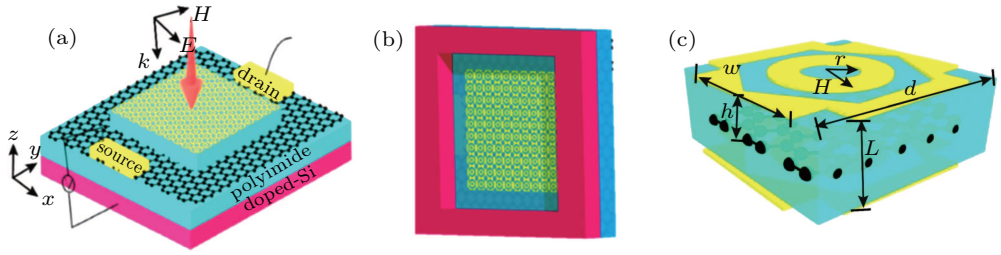


Fig. 1. (color online) Illustration of a metamaterial with graphene and the structural design. (a) Schematic illustration of the periodic arrangement of the unit cell. (b) Bottom structure design of the metamaterial. (c) Structural design of an individual unit cell.

The spacing between the top layer and the monolayer graphene sheet is defined as h. In the simulation, the real part of the permittivity and the loss tangent for PI are 3.1 and 0.05, respectively, when the center frequency is 5 THz.[24] Figure 1(c) shows the pattern design of the top metal film, which is made up of a cross-like pattern Boolean with a hexagonal hole inside and a circular ring at the center. The corresponding structural parameters are $d = 22$ μm, $w = 18$ μm, $r = 3$ μm, $R = 8$ μm, and $L = 10$ μm. To investigate the transmission spectra of the proposed filters, the THz transmission property was studied using the CST microwave studio. In the simulation, the incident THz waves of the metamaterial were along the z-axis to permeate the top layer of MGMs. The boundary conditions of PEC and PMC for the unit cell of the MGMs were simultaneously set along the x and y directions, respectively. Then, we simulated the THz beams from 2.0 THz to 8.0 THz with a resolution of 0.03 THz.

3. Mathematical model for control kinetics

Table 1 presents the five different mathematical models that can be used to describe the control process of the 3 dB bandwidth or the center frequency for the dynamic tuning passband filter. The best mathematical model for depicting the control process of the 3 dB bandwidth or the center frequency was chosen based on its statistical parameters, which include the root mean square error (E_{RMS}), reduced mean square of the deviation (χ^2), and the coefficient of correlation (R^2). In other words, these statistical parameters were applied as the primary criteria to select the mathematical model that best predicts the variation in the 3 dB bandwidth or the center frequency as the E_F was varied. More specifically, a higher R^2 value and lower E_{RMS} and χ^2 values were selected as the criteria for the goodness of fit for the transmission spectra.[25–27] In addition, E_{RMS} gives the deviation between the predicted and simulation values; R^2 gives the predictive power of the model relative to the control behavior of the filter, and its highest value is 1. To determine the superior mathematical model for describing the control process of the 3 dB bandwidth or the center frequency, linear and non-linear regression analyses were implemented to estimate the coefficients and parameters of the five mathematical models. The simulated 3 dB bandwidth, the predicted 3 dB bandwidth, the simulated center frequency, and the predicted center frequency were subjected to one-way analyses of variance (ANOVA). The statistical parameters (E_{RMS}, χ^2, and R^2) were calculated as follows:[28–30]

$$E_{RMS} = \sqrt{\frac{1}{N}\sum_{i=1}^{N}(f_{pre,i} - f_{sim,i})^2}, \tag{1}$$

$$\chi^2 = \frac{\sum_{i=1}^{N}(f_{sim,i} - f_{pre,i})^2}{N - n}, \tag{2}$$

$$R^2 = \frac{\sum_{i=1}^{N}(f_i - f_{pre,i})\sum_{i=1}^{N}(f_i - f_{sim,i})}{\sqrt{\left[\sum_{i=1}^{N}(f_i - f_{pre,i})^2\right]\left[\sum_{i=1}^{N}(f_i - f_{sim,i})^2\right]}}, \tag{3}$$

where $f_{sim,i}$ is the i-th simulation 3 dB bandwidth or center frequency, $f_{pre,i}$ is the i-th predicted 3 dB bandwidth or center frequency, N is the number of observations, n is the number

of constants in the mathematical model, and i is the number of terms.

Table 1. Mathematical models applied to control the 3 dB bandwidth or the center frequency.

Model	Model equation
Gaussamp	$f(E_F) = a + b\,e^{[-0.5((E_F-c)/m)^2]}$
DoseResp	$f(E_F) = a + \frac{b-a}{1+10^{m(c-E_F)}}$
Parabolic	$f(E_F) = a + bE_F + cE_F^2$
Quartic	$f(E_F) = a + bE_F + cE_F^2 + dE_F^3 + mE_F^4$
Line	$f(E_F) = a + bE_F$

In Table 1, f represents the 3 dB bandwidth or the center frequency of the graphene metamaterial filter, E_F represents the Fermi energy level of graphene, and a, b, c, d, and b represent the coefficients of the five different mathematical models.

4. Results and discussion

4.1. Effect of structural parameters on the filter

The THz transmission responses of the proposed filter with different spacing h are shown in Fig. 2(a). As seen in Fig. 2(a), the THz transmission response of MGMs increased as h was varied from 1 μm to 5 μm when the E_F was set to 0.3 eV. The THz transmission responses of MGMs reveal two resonant responses, namely, f_a and f_b, which can be described by a plasmonic dipole resonance induced by the incident THz field.[19,31] To a certain extent, a higher value of h is more beneficial for enhancing transmission responses. The transmissivity was increased by 13% and 19.9% at f_a and f_b, respectively, with the increase of h from 1 μm to 5 μm. To illustrate the THz transmission behavior of MGMs at a fixed E_F, we simulated the unit cell structure without metallic patterns, remaining graphene and PI substrates (GPs). The spacing h was tuned from 1 μm to 9 μm to determine the effects of the geometric parameter on the transmission spectra, and the results are shown in Fig. 2(b). From Fig. 2(b), it can been seen that the transmissivity of the GPs was significantly affected by the spacing h. In particular, the transmission responses with $h = 5$ μm were the strongest, whereas for $h = 1$ μm, the transmission responses were the weakest. In other words, when the location of the graphene sheet was in the middle of the PI substrate, the transmissivity was the highest. By contrast, when the graphene sheet was closer to the top or bottom layer, the transmission efficiency became weaker. Compared to the transmissivity of the GPs, the transmissivity of MGMs is related to the location of graphene in the PI. Furthermore, in order to determine the effect of the other unit cell structural parameters of the metamaterial, we discussed the effect of the other structural parameters in more detail. As can be seen from Fig. 2(c), we first defined the width of the metal ring $\Delta R = R - r$, where R is the outside radius and r is the inside radius of the metal ring. When ΔR was fixed at 3 μm, by changing R from 4 μm to 8 μm and r from 1 μm to 5 μm under a fixed graphene E_F of 0 eV, we found that the bandwidth of the filter widened with the increase in the metal ring size. In addition, the transmission of the metamaterial filter also increased with the increase in the metal ring size (Fig. 2(c)). A possible explanation for this might be that, as the size of metal ring increases, the loss of structures reduces. On the other hand, we also studied the effect of ΔR on the transmission efficiency; R was fixed at 7 μm, and r was changed from 2 μm to 6 μm. It can be seen from Fig. 2(d) that the bandwidth of the filter widened when r was increased from 2 μm to 6 μm. At the same time, the transmission increased from 0.67 to 0.74, which implies that the growing linewidth of the metal ring may result in a decrease in transmission as well. Furthermore, we also found that the parameter w and the temperature have little effect on the transmission of our designed filter, as shown in Figs. 2(e) and 2(f). Thus, the difference in transmission response can be deduced from Figs. 3(a)–3(c), which show the current density distribution of the graphene layer with $h = 1$ μm, 3 μm, and 5 μm in MGMs. Evidently, the surface current density decreased as h was increased from 1 μm to 5 μm. Comparing Fig. 3(a) and Fig. 4(a), figure 4(a) shows a strong coupling effect between the graphene film and Au film when $h = 1$ μm. Consequently, the current density and the dissipative power density in graphene can be determined by the following equation:[32]

$$\boldsymbol{J}_g = \sigma_g \boldsymbol{E}_{res}, \tag{4}$$

$$W = \sigma_g ||\boldsymbol{E}_{res}||^2, \tag{5}$$

where $\boldsymbol{J}_B$ is the current density, σ_g is the conductivity of graphene, W is the dissipative power density, and $\boldsymbol{E}_{res}$ is the resonant electric field. Both Eqs. (4) and (5) imply that the current density $\boldsymbol{J}_g$ is proportional to the resonant electric field $\boldsymbol{E}_{res}$. The dissipative power density W is represented by a quadratic function of the resonant electric field when the conductivity of graphene is fixed. When h was tuned from 5 μm to 1 μm, a resonant electric field enhancement effect was observed with an increase in current density, and thus, W greatly increased. As a result, the transmission responses were damped by the dissipation of the graphene layer. Therefore, the noticeable difference in transmission response at 28 THz had a strong relationship with the coupling effect between the GPs. In addition, when the spacing h was changed from 5 μm to 1 μm, the coupling effect between the graphene film and metal film became stronger, and an evident coupling effect was observed between the graphene film and the metal film at 1 μm.

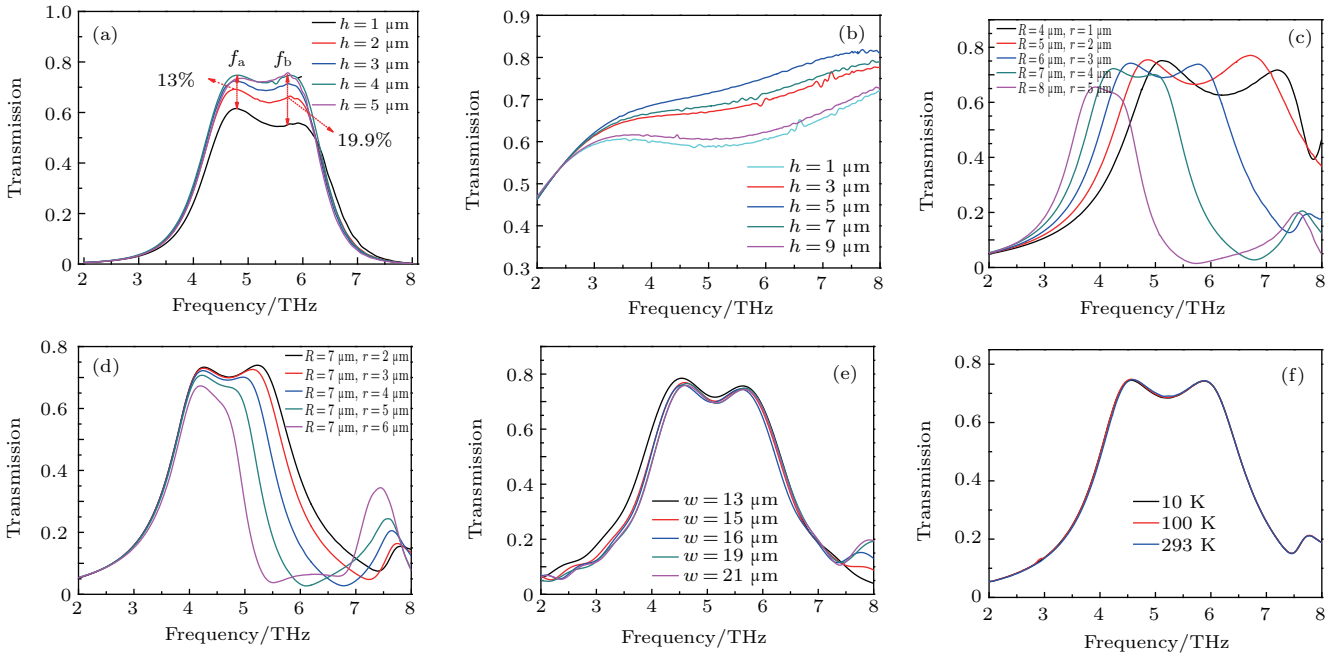


Fig. 2. (color online) (a) Transmission spectra of MGMs treated with different spacing h. (b) Transmission spectra of the unit cell structures consisting of graphene and PI substrates (GPs) with different spacing h. (c) Dependence of transmission on different ΔR values. (d) Dependence of transmission on different r values of the metal ring when the outside radius is fixed at 7 μm. (e) Effect of w on the transmission spectra of MGMs. (f) Effect of graphene temperature on the transmission spectra of MGMs.

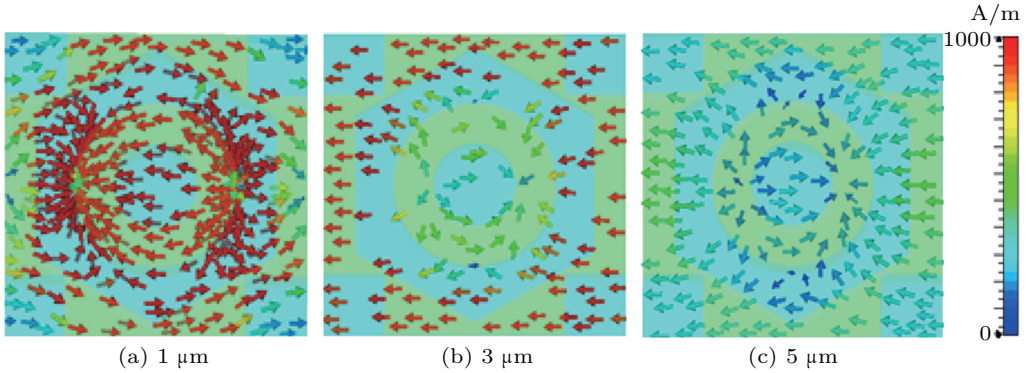


Fig. 3. (color online) Distribution of the surface current density in the graphene sheet with different spacing h: (a) 1 μm, (b) 3 μm, and (c) 5 μm.

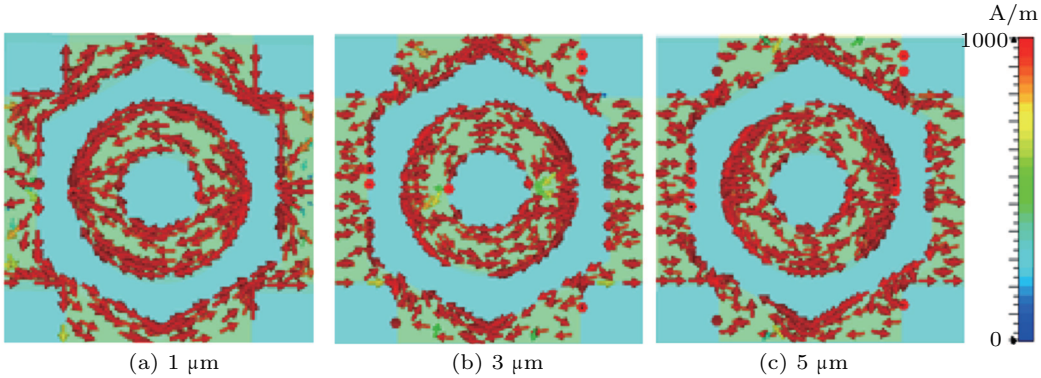


Fig. 4. (color online) Distribution of the surface current density in the top Au film with different spacing h: (a) 1 μm, (b) 3 μm, and (c) 5 μm.

4.2. Influence of different combination models on transmission

As shown in Figs. 5(a) and 5(b), the spacing between the top-layer metal film and the monolayer graphene sheet is defined as h; in the figures, no-graphene indicates that graphene is not present in the unit cell. In the no-graphene metamaterial model, $h = 0$ μm indicates that the monolayer graphene sheet was located on the top metal film of the unit cell, an arrangement defined as the top-coplanar hybridization of graphene with the metamaterial model. A spacing of $h = 10$ μm in-

dicates that the monolayer graphene sheet was located on the bottom metal film of the unit cell, an arrangement that is defined as the bottom-coplanar hybridization of graphene with the metamaterial model. The different values of spacing h realize different hybrid models. To further evaluate the relationship between the spacing h and the THz transmission responses, the effect of the spacing h is shown in Fig. 5(a), in which the E_F of graphene is fixed at 0.3 eV and the other parameters are constant. The simulation results indicated that the change in spacing h significantly influenced the transmissions. When the spacing $h = 5$ μm, the transmission spectra showed better flatness and strong transmission intensity. In fact, increases of 41% and 63.16% were observed in the THz transmission at f_a and f_b, respectively, in comparison to the transmission with the spacing $h = 0$ μm. On the other hand, for the spacing $h = 0$ μm and $h = 10$ μm, the transmission spectra almost overlapped and had similar profiles in Fig. 5(a). In addition, figure 5(b) shows that the transmission spectrum when the spacing $h = 5$ μm had the most similar profile to that of the spectrum of the structure with no graphene. The transmission showed an approximate decrease of 3.6% and 1.73% at f_a and f_b, respectively, in comparison to that of the structure with no graphene, whereas a slight blue shift occurred when E_F was fixed at 0 eV. Moreover, the decrease in the transmission intensity with $h = 0$ μm was the most evident; the transmission intensity decreased by approximately 80.3% and 69.95% at f_a and f_b, respectively, in comparison to that of the structure with no graphene. Figures 5(c)–5(e) show the resonance electric field distributions of different combination models at 4.49 THz, 4.48 THz, and 4.24 THz for the PI substrate, respectively. Compared to the resonance electric field distribution, as shown in Figs. 5(c) and 5(d), the electric field intensity distributions under the two conditions are very similar when the spacing $h = 5$ μm without graphene in the unit cell. Meanwhile, as shown in Fig. 5(e), the monolayer graphene sheet was located on the top metal film of the unit cell; thus, it could generate positive and negative charge redistributions, leading to an increase in the electric field intensity. Based on Eq. (5), the decrease in THz transmission for different combination models is due to the enhancement in the electric field intensity. On the other hand, generally, the plasmon can be excited by the THz wave in monolayer graphene, and the nonlocal plasmon dispersion relation of monolayer graphene can be affected by a thick conductor owing to the coulomb couple. Based on Ref. [33], the nonlocal plasmon dispersion relation of monolayer graphene would be relevant to the various values of the distance between the monolayer graphene sheet and the conductor surface. Specifically, the two plasmon branches of the monolayer evolve into a merged spectral line and the surface plasmon branch tends to be dispersionless as the separation is increased. However, as the monolayer graphene sheet was close to the surface of the conductor, i.e., when the distance between the surface and the layer became less than a certain critical value, the lower acoustic plasmon branch became overdamped. This conclusion can be suitably used to explain the phenomenon observed when the monolayer graphene sheet was located on the metal film of the unit cell ($h = 0$, 10 μm) in our work. In other words, when $h = 0$, 10 μm, based on the results of Ref. [33], the overdamping of the plasmon branch occurs in the monolayer graphene of the metamaterials filter; therefore, the transmission of the metamaterials filter decreased greatly. In summary, the effect of the above mentioned parameters on the transmission of our designed metamaterials filter has been discussed. These results show the remarkable transmission variation in spectral response caused by changing the value of spacing h.

4.3. Tunability dependence of transmission on Fermi energy

The transmission spectra of MGMs can be dynamically tuned via the tuning of the E_F of graphene. The transmission spectra under different E_F values when the spacing $h = 5$ μm are shown in Fig. 6(a). The transmission spectra exhibit significant tunable filtering properties, and two resonant frequencies contained the resonance frequencies f_a and f_b. When the Fermi energy increased from 0 to 0.25 eV, f_a blue shifted from 4.478 THz to 4.64 THz, accompanied by a decrease in the transmission efficiency from 84.6% to 76.2%. When the E_F was over 0.25 eV, f_a disappeared and only f_b was left. The THz resonance response at both f_a and f_b became smooth with an increase in E_F from 0 to 0.75 eV. To obtain a clearer explanation, we defined a 3 dB bandwidth $\Delta f = f_i - f_h$ to characterize such a passband transmission and demonstrate the center frequency as f_0. To illustrate the dynamic tuning property of graphene for the proposed filter, the center frequency f_0 and Δf as a function of E_F are exhibited in Fig. 6(b), respectively. As E_F increased from 0 to 0.75 eV, f_0 increased from 5.04 THz to 5.71 THz, accompanying a decline in Δf from 1.824 THz to 0.0144 THz. On the other hand, the frequency f_i blue shifted from 4.172 THz to 5.642 THz, whereas f_h shifted towards lower frequencies (red shifts) from 5.996 THz to 5.786 THz. Moreover, when the Fermi energy was set from 0.05 THz to 0.75 eV, the THz transmission of MGMs at 4.48 THz decreased from 84.6% to 35.4%, and the modulation depth in the THz transmission reached 49.2%. Figure 6(c) shows the transmission spectrum of GPs when $h = 5$ μm. As shown in the figure, when the frequency ranged from 2 to 4 THz, the transmission spectrum of GPs showed an obvious change, and the transmission in the frequency range decreased when the Fermi energy was increased. However, as the frequency ranged from 4 THz to 8 THz, the transmission spectrum at different E_F values achieved an aggregating state. Considering the tuning

mechanism, as the transmission spectra of MGMs are influenced by GPs, when the frequency changed from 2 THz to 4 THz, the transmission of MGMs declined much faster than that when the frequency was changed from 4 THz to 8 THz. Furthermore, the transmission spectrum of MGMs had more shifts between 2 THz and 4 THz than between 4 THz and 8 THz. In other words, the shift in the transmission spectrum of MGMs is determined by the changing trend of the transmission spectrum of GPs. To verify the coupling effect of GPs, we simulated a transmission spectrum of the single layer graphene at a Fermi energy between 0.15 eV to 0.75 eV, and the results are shown in Fig. 6(d).

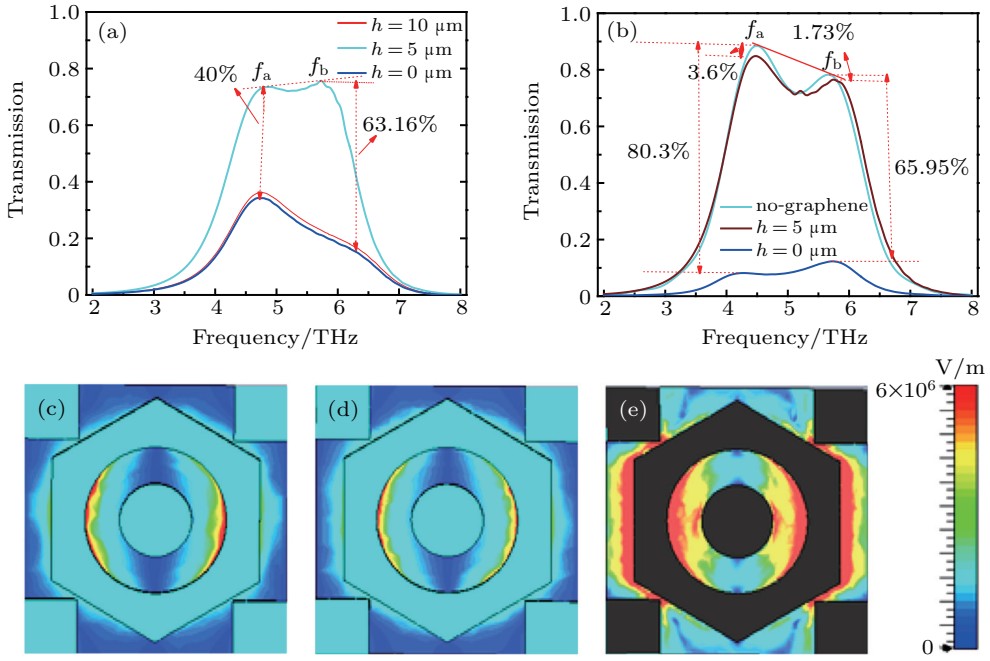


Fig. 5. (color online) Transmission spectra of the proposed filter with different combination models. (a) Effect of the transmission spectra when E_F is 0.3 eV. (b) Effect of the transmission spectra when the E_F was set at 0 eV. (c) Distribution of the resonant electric field with no graphene. (d) Distribution of the resonant electric field with $h = 5$ μm. (e) Distribution of the resonant electric field with $h = 0$ μm.

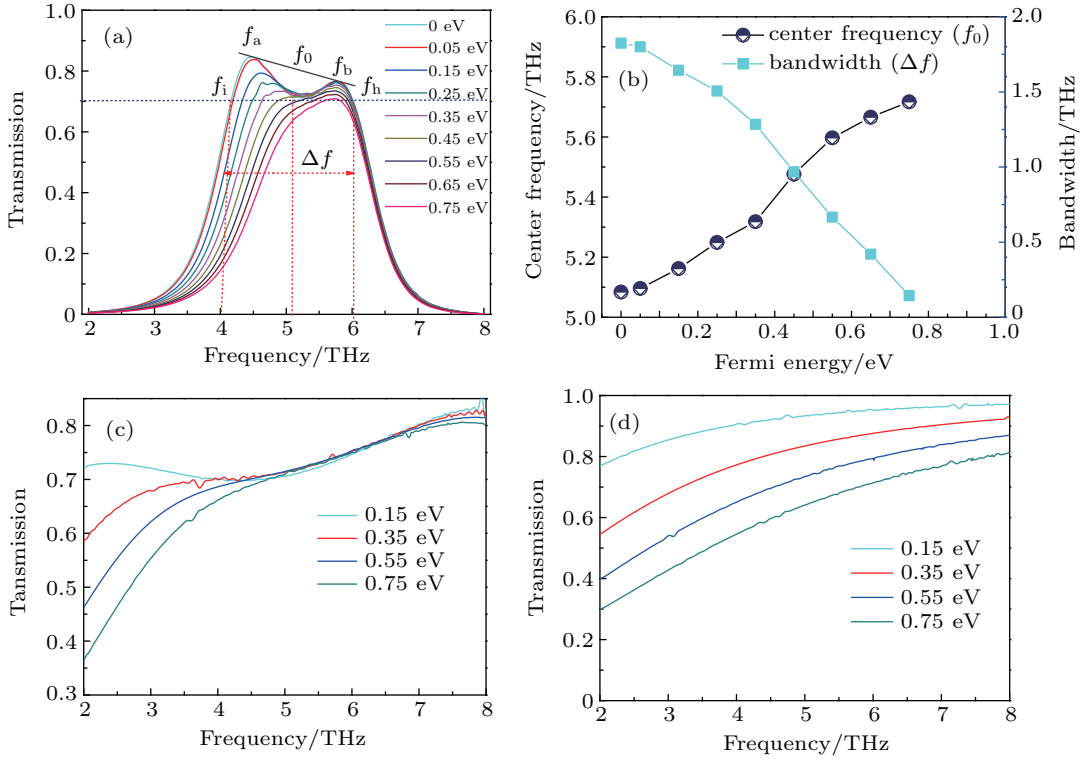


Fig. 6. (color online) Transmission spectra of the proposed filter treated with different Fermi level energies. (a) Transmission spectra of MGMs. (b) Effect of f_0 and Δf. (c) Transmission spectra of GPs. (d) Transmission spectra of a single graphene sheet.

By comparing Fig. 6(c) and Fig. 6(d), we can make sure that the transmission spectrum of GPs is caused by the coupling effect of GPs with different E_F values. Furthermore, figures 7(a)–7(d) show the electric field distribution of a graphene sheet with different E_F values at 3.86 THz. As the E_F was tuned from 0.15 eV to 0.75 eV, the electric field density became stronger in the middle region of graphene, and an emergence of small regions for very weak electric field intensities on the edge of graphene was observed. Figures 8(a)–8(d) show the electric field distribution of the top-layer Au film. As the Fermi energy was changed from 0.15 eV to 0.75 eV, a strong electric field density emerged on the edge of the internal ring and regular hexagon thin plate; however, as the electric field intensity was very weak near the apex of the hexagon, we can infer that a coupling effect between metal films and the graphene was present. In addition, more THz in graphene was lost because regions of stronger electric field intensities were much larger than those of weaker electric field intensities. This observation can be explained by the dissipative power density W as a function of the resonant electric field $\boldsymbol{E}_{res}$ and the conductivity of graphene (Eqs. (4) and (5)). As the Fermi energy was tuned from 0.15 eV to 0.75 eV, the resonant electric field and conductivity due to graphene enhancement were observed with increases in E_F; then as the dissipative power density W increased, the transmission was damped by dissipation in the graphene layer caused by varying of the Fermi energy. Therefore, the transmission shows a strong dependence on the Fermi level. The relationship between Fermi energy and the conductivity of graphene can be explained by Kubo's formalism. In the THz region, the carrier intraband transitions play a key role in influencing the optical conductivity in graphene.[23] The optical conductivity of graphene is dominated by intraband and interbond transitions. It can be modeled using Kubo's formalism[8,34,35]

$$\sigma(\omega,\Gamma,\mu_c,T) = \sigma_{inter}(\omega,\Gamma,\mu_c,T)+\sigma_{intra}(\omega,\Gamma,\mu_c,T), \tag{6}$$

$$\sigma_{inter}(\omega,\Gamma,\mu_c,T) = \frac{ie^2(\omega+i2\Gamma)}{\pi\hbar^2}\int_0^\infty \frac{f_d(-\xi)-f_d(\xi)}{(\omega+i2\Gamma)^2-4(\xi/h)^2}\,d\xi, \tag{7}$$

$$\sigma_{intra}(\omega,\Gamma,\mu_c,T) = \frac{ie^2}{\pi\hbar^2(\omega+i2\Gamma)}\int_0^\infty \xi\left(\frac{\partial f_d(\xi)}{\partial\xi}-\frac{\partial f_d(-\xi)}{\partial\xi}\right)d\xi, \tag{8}$$

$$f_d(\xi) = \frac{1}{\exp((\xi-\mu_c)/(k_BT))+1}, \tag{9}$$

where ω is the angular frequency, Γ is the scattering rate, μ_c is the chemical potential, T is the environment temperature, $f_d(\xi)$ is the Fermi–Dirac distribution, e is the electron charge, $\hbar$ is the reduced Planck's constant, and ξ is the photon energy. The scattering rate Γ and the environment temperature T are respectively set to be 0.0001 eV and 293 K. The chemical potential and the carrier concentration of graphene can be described as follows:[36,37]

$$\mu_c = \hbar v_F(\pi n)^{1/2}, \tag{10}$$

$$n = \varepsilon_0\varepsilon V_g/ed, \tag{11}$$

where μ_c is the chemical potential, n is the carrier concentration, v_F is the Fermi velocity of the graphene, V_g is gate voltage, ε_0 and ε are the free space and insulated substrate material permittivity, respectively, and d is the thickness of the insulated substrate material.

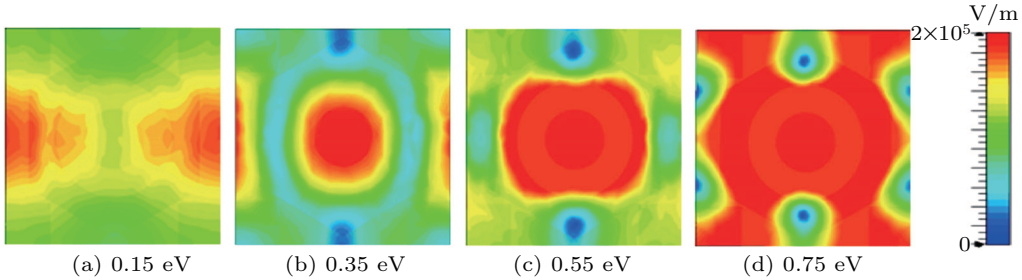


Fig. 7. (color online) Distribution of resonant electric field in the graphene sheet treated with different Fermi level energies.

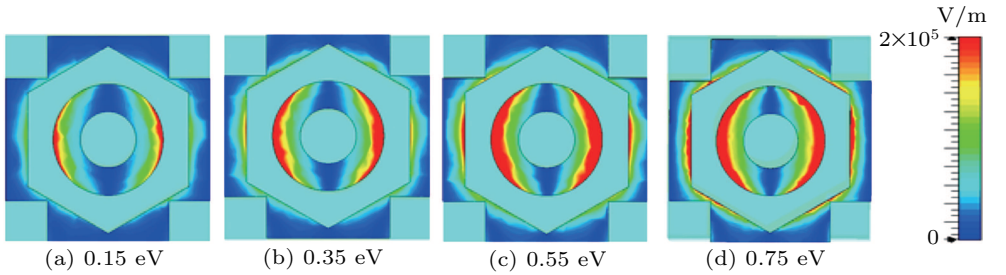


Fig. 8. (color online) Distribution of resonant electric fields on the top-layer Au film treated with different Fermi energies.

4.4. Selection of the superior mathematical model

4.4.1. Best mathematical model for control of the 3 dB bandwidth

The results of statistical analyses on the modeling of the 3 dB bandwidth for the THz passband filter are listed in Table 2. Generally, the values of R^2, $R_{\rm MES}$, and χ^2 for the five different mathematical models were 0.97576 to 0.9970, 0.04683 to 0.18872, and 0.00091 to 0.01285, respectively (Table 2). Based on the evaluation criteria mentioned above, the superior mathematical model that suitably depicted the control process of the 3 dB bandwidth was chosen as the one with the highest R^2 value and the lowest χ^2 and $R_{\rm MES}$ values. Table 2 confirms that the values of R^2 for the models were greater than 0.95, indicating that the five different mathematical models had good fitness.[29] However, the line model had high $R_{\rm MES}$ and χ^2 values, which made it a weaker model in comparison to other mentioned models for depicting the control process of the 3 dB bandwidth. In addition, Table 2 shows that the DoseResp model provided the highest value of R^2 (0.9970), and the lowest values of χ^2 (0.9970) and $R_{\rm MES}$ (0.04683) for control of the 3 dB bandwidth. Accordingly, the DoseResp model was selected as the superior mathematical model to represent the behavior for control of the 3 dB bandwidth. In order to further demonstrate that the DoseResp model was the most suitable mathematical model for depicting the control process of the 3 dB bandwidth, the predicted 3 dB bandwidth by the DoseResp model and the simulated 3 dB bandwidth were compared at different random $E_{\rm F}$ values in the range 0 to 0.8 eV. Figure 9(b) shows the evolution of the simulated 3 dB bandwidth and predicted 3 dB bandwidth by the DoseResp model as a function of $E_{\rm F}$ in the range 0 to 0.8 eV. As can be seen, the predicted 3 dB bandwidth data by the DoseResp model is almost the same as the simulated data. An ANOVA showed that no significant difference ($p > 0.001$) existed between the predicted 3 dB bandwidth and the simulated data, thus strengthening the view that the DoseResp model could perfectly predict the variation in the 3 dB bandwidth when the $E_{\rm F}$ was changed, as an excellent conformity between the simulated and the predicted 3 dB bandwidth was observed. Therefore, the DoseResp model can be successfully applied to regulate and control the 3 dB bandwidth of a THz passband filter. In addition, the values of a, b, c, and m for the DoseResp model were 0.2439, 1.8812, 0.4924, and -2.9535, respectively (Table 2). a and b are the bottom and top asymptotes, respectively, c is the value at the center of the DoseResp value, and m is the hill slope. From the DoseResp model applied for controlling the process of the 3 dB bandwidth ($f = -0.2439 + 2.1251/[1+10^{-2.9535(0.4924-E_{\rm F})}]$, it was found that the 3 dB bandwidth of the THz passband filter could be regulated from -0.2439 to 1.8812. Moreover, near the center of the DoseResp model, where the value of c is 0.4924, the rate of change for the 3 dB bandwidth is higher than that at both ends (Fig. 9(b)).

Table 2. Results of statistical analyses on the modeling of 3 dB bandwidth and $E_{\rm F}$.

Model	Model coefficients					Statistical parameters		
	a	b	c	d	m	$R_{\rm MES}$	R^2	χ^2
DoseResp	–0.2439	1.8812	0.4924		–2.9535	0.04683	0.9970	0.00091
Gaussamp	1.8562	–1.7822	0.8033		0.2984	0.04738	0.9969	0.00093
Quartic	1.8246	–0.9904	2.7669	–17.555	15.474	0.04737	0.9967	0.00101
Parabolic	1.8529	–0.8419	–2.4034	–0.6566		0.08353	0.9911	0.00222
Line	2.0348	–2.5053				0.18872	0.9576	0.01285

4.4.2. Best mathematical model for control of the center frequency

Table 3 lists the coefficients and parameters of the five mathematical models for controlling the center frequency. The values of R^2, $R_{\rm MES}$, and χ^2 range from 0.978997 to 0.999801, 0.003721 to 0.041821, and 0.024805 to 3.086183, respectively (Table 3). From Table 3, it can be concluded that the line model is also a weak model in comparison to the other mentioned models for depicting the control process of the center frequency. On the other hand, the quartic model is the most suitable mathematical model for depicting the control process of the center frequency as its statistical parameters meet the criteria for selecting the most suitable mathematical model. Figure 9(a) shows the evolution of the simulated and predicted center frequency by the quartic model as a function of $E_{\rm F}$ in the $E_{\rm F}$ range 0 to 0.8 eV. As shown in the figure, the predicted center frequency data by quartic model is almost equal to the simulated data. An ANOVA showed that significant differences ($p > 0.001$) did not exist between the predicted center frequency data and the simulated data, indicating that an excellent conformity exists between the simulated and the predicted center frequencies. Therefore, the quartic model can successfully describe the variation in the center frequency of a terahertz passband filter.

Table 3. Results of statistical analyses on the modeling of the center frequency and $E_{F.}$

Model	Model coefficients						Statistical parameters		
	a	*b*	*c*	*d*	*m*		R_{MES}	R^2	χ^2
Quartic	5.0643	1.0315	–4.5427	14.8646	–12.341	0.02372	0.9947	0.00025	
Gaussamp	5.0707	0.6397	0.7246		0.2777	0.03449	0.9923	0.00049	
Doseresp	5.0601	5.8120	0.4299		3.1667	0.03252	0.9908	0.00044	
Parabolic	5.0545	0.6572	0.4999			0.05112	0.9789	0.00101	
Line	5.0545	1.0027				0.06204	0.9710	0.00139	

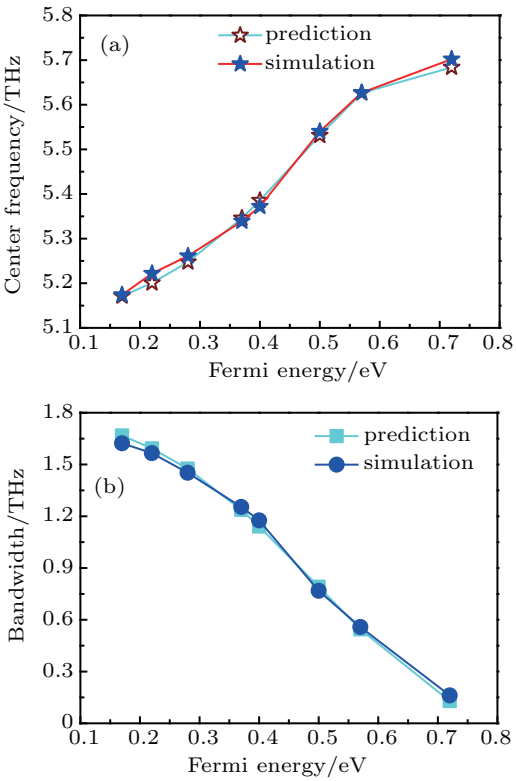


Fig. 9. (color online) Comparison of simulated data with predicted data obtained by the models at different E_F values of graphene. (a) Center frequencies. (b) 3 dB bandwidths.

5. Conclusion

We have proposed and evaluated a dynamic tuning passband filter based on the sandwiched structure of graphene and metamaterials in the THz region. The results showed that, initially, the transmission spectrum of MGMs had more shifts between 2 THz and 4 THz, whereas few changes occurred between 4 THz and 8 THz via tuning the Fermi energy of graphene. The remarkable spectral response variation was caused by changing the value of spacing *h*; when the spacing *h* reached 5 μm, the highest transmission for MGMs was acquired. These results indicate a desirable performance of the proposed structure in the THz region, particularly in terms of tunability. We envision that the dynamically tunable THz passband filter may be useful in future all-integrated graphene plasmonic THz devices and communication systems. Among the five equations considered in this study, the DoseResp model gave excellent fits for all simulated 3 dB bandwidths, and the Quartic model can be successfully used to describe the variation in the center frequency of a THz passband filter.

References

[1] Federico Valmorra G S, Maissen C, Fu W, Schönenberger C, Choi J W, Park H G, Beck M and Faist J 2013 *Nano Lett.* **13** 3193
[2] Li C, Zhou Q, Shi Y, Yang Z, Shi L and Zhang C 2017 *Opt. Commun.* **391** 77
[3] Fu Y N, Zhang J Y, Qun X, Li Y H and Yu J Y 2017 *Acta Phys. Sin.* **66** 180701 (in Chinese)
[4] Liu J F, Zhou Q L, Shi Y L, Li L, Zhao D M and Zhang C L 2012 *Acta Phys. Sin.* **61** 048101 (in Chinese)
[5] Zhi H L, Zhou T, Cao J and Tao H 2017 *IEEE 30th International Conference on* 974
[6] Peter F and Siegel H 2004 *IEEE T. Microw. Theory* **52** 2438
[7] Walther M, Plochocka P, Fischer B, Helm H and Uhd Jepsen P 2002 *Biopolymers* **67** 310
[8] Jiang L H, Wang F, Liang R, Wei Z, Meng H, Dong H, Cen H, Wang L and Qin S 2017 *Plasmonics* **13** 525
[9] Withayachumnankul W and Abbott D 2009 *IEEE Photon. J.* **1** 99
[10] Oliver Paul C I, Reinhard B, Remigius, Zengerle and Beigang R 2008 *Opt. Exp.* **16** 6736
[11] Chen H T, Taylor A J and Yu N 2016 *Rep. Prog. Phys.* **79** 076401
[12] Shen X P, Cui T J and Ye J X 2012 *Acta Phys. Sin.* **61** 058101 (in Chinese)
[13] Wang Z Y, Qiu J P, Chen H, Mo J J and Yu F X 2017 *Chin. Phys. B* **26** 094207
[14] Guo J J, Huang W X and M S 2017 *Chin. Phys. B* **26** 124211
[15] Nikolaenko A E, Papasimakis N, Atmatzakis E, Luo Z, Shen Z X, De Angelis F, Boden S A, Di Fabrizio E and Zheludev N I 2012 *Appl. Phys. Lett.* **100** 181109
[16] Ou, J Y, Plum E, Jiang L and Zheludev N I 2011 *Nano Lett.* **11** 2142
[17] Yeh S G, Monorchio A, Prati E, Costa F, Huang T Y and Yen T J 2012 *Opt. Exp.* **20** 7580
[18] Li P, Hu F, Wang Z, Jiang W, Wang Y E and Chen Y 2017 *Opt. Commun.* **392** 263
[19] Wang X Z, Zhu H H and Liu Z G 2017 *Opt. Commun.* **396** 236
[20] Liang L J, Jin B B and W U J B 2013 *Sci. Chin. Inform Sci.* **56** 120412
[21] Giovannetti G, Khomyakov P A, Brocks G, Karpan V M, Brink and Kelly P J 2008 *Phys. Rev. Lett.* **101** 026803
[22] Mousavi S H, Kholmanov I, Alici K B, Purtseladze D, Arju N, Tatar K, Fozdar D Y, Suk J W, Hao Y, Khanikaev A B, Ruoff R S and Shvets G 2013 *Nano Lett.* **13** 1111
[23] Sensale-Rodriguez B, Yan R, Kelly M M, Fang T, Tahy K, Hwang W S, Jena D, Liu L and Xing H G 2012 *Nat. Commun.* **3** 780
[24] Liang L, Jin B, Wu J, Huang Y, Ye Z, Huang X, Zhou D, Wang G, Jia X, Lu H, Kang L, Xu W, Chen J and Wu P 2013 *Appl. Phys. B* **113** 285
[25] Chiang Y J, Yang C S, Yang Y H, Pan C L and Yen T J 2011 *Appl. Phys. Lett.* **99** 191909
[26] Kaleta A and Górnicki K 2010 *Energy Convers Manag.* **51** 2967
[27] Menges, H O and Ertekin C 2006 *J. Food Eng.* **77** 119
[28] Dinani S T, Hamdami N and Shahedi M 2014 *Energy Conversion Managem.* **86** 70
[29] Yang M S and Ding C J 2016 *Springerplus* **5** 909
[30] Ding C, Lu J and Song Z 2015 *PLoS One* **10** 0124077
[31] Shahhoseini R, Ghorbani H and Karimi S R 2013 *Dry Technol.* **31** 1020
[32] Pendry J B, Robbins D J and Stewart W J 1999 *IEEE T. Microw. Theory* **47** 2075
[33] Godfrey G, Andrii I and Horing N J M 2015 *Phys. Rev. B* **91** 235416
[34] Yan P T, Zou H, Koschny T and Soukoulis M 2012 *Opt. Express* **20** 12198
[35] Correas-Serrano D, Perruisseau-Carrier J and Alvarez-Melcon A 2014 *IEEE T. Nano. Technol.* **13** 1145
[36] Hanson G W 2008 *J. Appl. Phys.* **103** 1
[37] Ju L, Geng B, Horng J, Girit C, Martin M, Hao Z Bechtel H A, Liang X, Zettl A, Shen Y R and Wang F 2011 *Nat. Nanotechnol.* **6** 630